

## A generalized plasma dispersion function for electron damping in tokamak plasmas

L. A. Berry, E. F. Jaeger, C. K. Phillips, C. H. Lau, N. Bertelli, and D. L. Green

Citation: *Physics of Plasmas* **23**, 102504 (2016); doi: 10.1063/1.4964766

View online: <http://dx.doi.org/10.1063/1.4964766>

View Table of Contents: <http://scitation.aip.org/content/aip/journal/pop/23/10?ver=pdfcov>

Published by the **AIP Publishing**

---

### Articles you may be interested in

[Resonance in fast-wave amplitude in the periphery of cylindrical plasmas and application to edge losses of wave heating power in tokamaks](#)

*Phys. Plasmas* **23**, 070702 (2016); 10.1063/1.4954899

[Identification of new turbulence contributions to plasma transport and confinement in spherical tokamak regime](#)

*Phys. Plasmas* **22**, 102509 (2015); 10.1063/1.4933216

[On the non-stiffness of edge transport in L-mode tokamak plasmas](#)

*Phys. Plasmas* **21**, 055906 (2014); 10.1063/1.4876612

[Monte Carlo orbit/full wave simulation of ion cyclotron resonance frequency wave damping on resonant ions in tokamaks](#)

*Phys. Plasmas* **12**, 072505 (2005); 10.1063/1.1935387

[High-bootstrap, noninductively sustained electron internal transport barriers in the Tokamak à Configuration Variable](#)

*Phys. Plasmas* **12**, 056124 (2005); 10.1063/1.1896953

---



*High Peak Power Femtosecond Lasers*

- Peak Powers to 1PW
- Contrast <math>< 1:10^{12}</math>
- Advanced Control System (GUI)

Amplitude Laser Group  
Continuum | Amplitude Technologies | Amplitude Systèmes  
140 Baytech Drive, San Jose, CA 95134, USA

**Continuum**<sup>®</sup>  
[www.continuumlasers.com](http://www.continuumlasers.com)

# A generalized plasma dispersion function for electron damping in tokamak plasmas

L. A. Berry,<sup>1</sup> E. F. Jaeger,<sup>1,a)</sup> C. K. Phillips,<sup>2</sup> C. H. Lau,<sup>3</sup> N. Bertelli,<sup>2</sup> and D. L. Green<sup>3</sup>

<sup>1</sup>XCEL Engineering, 1066 Commerce Park Dr., Oak Ridge, Tennessee 37830, USA

<sup>2</sup>Princeton Plasma Physics Laboratory, 100 Stellarator Rd., Princeton, New Jersey 08543, USA

<sup>3</sup>Oak Ridge National Laboratory, 1 Bethel Valley Rd., Oak Ridge, Tennessee 37831, USA

(Received 21 August 2016; accepted 29 September 2016; published online 14 October 2016)

Radio frequency wave propagation in finite temperature, magnetized plasmas exhibits a wide range of physics phenomena. The plasma response is nonlocal in space and time, and numerous modes are possible with the potential for mode conversions and transformations. In addition, diffraction effects are important due to finite wavelength and finite-size wave launchers. Multidimensional simulations are required to describe these phenomena, but even with this complexity, the fundamental plasma response is assumed to be the uniform plasma response with the assumption that the local plasma current for a Fourier mode can be described by the “Stix” conductivity. However, for plasmas with non-uniform magnetic fields, the wave vector itself is nonlocal. When resolved into components perpendicular ( $k_{\perp}$ ) and parallel ( $k_{\parallel}$ ) to the magnetic field, locality of the parallel component can easily be violated when the wavelength is large. The impact of this inconsistency is that estimates of the wave damping can be incorrect (typically low) due to unresolved resonances. For the case of ion cyclotron damping, this issue has already been addressed by including the effect of parallel magnetic field gradients. In this case, a modified plasma response ( $Z$  function) allows resonance broadening even when  $k_{\parallel} = 0$ , and this improves the convergence and accuracy of wave simulations. In this paper, we extend this formalism to include electron damping and find improved convergence and accuracy for parameters where electron damping is dominant, such as high harmonic fast wave heating in the NSTX-U tokamak, and helicon wave launch for off-axis current drive in the DIII-D tokamak. *Published by AIP Publishing.* [<http://dx.doi.org/10.1063/1.4964766>]

## I. INTRODUCTION

Radio frequency (RF) heating has been employed for a wide range of applications in magnetized fusion plasmas. Frequencies ranging from the ion cyclotron frequency  $\Omega_{ci}$  to below the lower hybrid frequency have been used. At the lower end of this range (typically  $1\Omega_{ci}$ – $3\Omega_{ci}$ ), heating has been observed in a wide range of experiments at the fundamental minority ion resonance, the second harmonic majority ion resonance, and the two-ion-hybrid mode conversion layer. At frequencies below  $\Omega_{ci}$ , the ions are magnetized, and interactions with the shear-Alfvén or compressional-Alfvén wave are possible. For frequencies well above the ion cyclotron frequency (typically above  $\sim 5\Omega_{ci}$ ), electron absorption dominates, and equilibrium currents can be driven when the waves are launched directionally. For example, current drive experiments using power in the range of  $\sim 5$ – $10\Omega_{ci}$  have been performed on the National Spherical Tokamak Experiment (NSTX)<sup>1</sup> and are also planned for NSTX-Upgrade (NSTX-U).<sup>2</sup> Experiments at still higher frequencies (harmonic numbers well over ten) are being evaluated for current drive applications on the DIII-D facility.<sup>3</sup> At these frequencies, the wave is described as a “helicon” or “whistler.” For some cases, geometric optics and ray-tracing algorithms can be used to examine basic propagation and absorption properties. However, traditional ray tracing does not readily allow exploration of antenna

geometry and fails to capture the effects of evanescent layers or mode conversion. Two-dimensional, full-wave simulations are required to include the finite temperature plasma response and to model the needed physics for tokamaks. A number of these codes have been described, and simulations compared for various ITER scenarios.<sup>4</sup>

Full-wave codes typically assume a plasma conductivity that is derived from the homogenous plasma response. For uniform plasmas where the RF electric field is expressed using a Cartesian Fourier basis set  $E(\mathbf{r}) = \sum_k E_k e^{i\mathbf{k}\cdot\mathbf{r}}$ , the RF current is given by  $J(\mathbf{r}) = \sum_k \sigma(\mathbf{k}, r) E_k e^{i\mathbf{k}\cdot\mathbf{r}}$ , where  $\sigma(\mathbf{k}, r)$  is the “Stix” conductivity tensor,<sup>5</sup> and the 3D wave vector  $\mathbf{k}$  has components parallel and perpendicular to the equilibrium magnetic field. If the magnetic field is not aligned with the coordinate axis, the wave vector components must be projected relative to the magnetic field,  $k_{\parallel} = \mathbf{k} \cdot \hat{\mathbf{b}}$ , and  $k_{\perp} = \mathbf{k} - k_{\parallel} \hat{\mathbf{b}}$ , where  $\hat{\mathbf{b}}$  is a unit vector in the direction of the magnetic field. Even when the plasma is not uniform and/or the coordinate system is not aligned with the equilibrium magnetic field, some form of the “local approximation” is used.<sup>6</sup> Although inexact, this approximation provides reasonable results that agree with experiments.

Serious numerical issues arise when the local parallel wave vector  $k_{\parallel}$  is sufficiently small that  $(\omega - n\Omega_{c,i})/k_{\parallel}v_{th} \gg 1$ . Here,  $\omega = 2\pi f$  is the wave frequency,  $n$  is the harmonic number, and  $v_{th}$  is the electron thermal velocity. In this case, the plasma response is reduced to that of a cold plasma, and the ion cyclotron resonance layers become very narrow and

<sup>a)</sup> Author to whom correspondence should be addressed. Electronic mail: [jaegeref@ornl.gov](mailto:jaegeref@ornl.gov).

difficult to resolve. For electrons where  $n=0$ , finite-temperature damping (e.g., Landau damping) is suppressed. Both of these situations can result in poor convergence and non-physical results. The origin of the variation in  $k_{\parallel}$  comes from up-shifts and down-shifts that follow from  $k_{\parallel} = \mathbf{k} \cdot \mathbf{b} = k_{\vartheta} b_{\vartheta} + \frac{n_{\varphi}}{R} b_{\varphi}$ , where the coordinates are poloidal angle  $\vartheta$  and toroidal angle  $\varphi$  in the tokamak case. For a given  $n_{\varphi}$  and  $k_{\vartheta}$ , the parallel wave number  $k_{\parallel}$  can be either up- or down-shifted, depending on the sign of  $b_{\vartheta}$ . The down-shift can easily lead to  $k_{\parallel} \approx 0$  locally. As resolution is increased, the poloidal mode numbers become progressively larger with a greater likelihood of  $k_{\parallel} \approx 0$ , leading to correspondingly poorer convergence—sometimes called “numerical pollution.”

When ion damping dominates, this issue has been addressed by considering the broadening that results from equilibrium magnetic field gradients.<sup>6</sup> This broadening has been used successfully in full-wave simulations such as TORIC<sup>7</sup> and AORSA.<sup>8</sup> When electron damping dominates, the electron Landau response becomes problematic. This effect is amplified when slow waves (possibly evanescent) are present in the solution because they are sensitive to errors in the parallel electric field caused by the poorly resolved electron response. When fast waves are dominant, these same errors may not impact the wave solution to the same degree because the parallel wave fields are smaller than the perpendicular fields by the electron to ion mass ratio.

In Section II, the effect of this “numerical pollution” is illustrated for parameters characteristic of shear Alfvén waves. Sections III and IV describe two approaches for improving the local approximation and enabling better resolution of electron absorption when the local  $k_{\parallel}$  is small. Section V applies this improved electron response to full wave simulations in Alcator CMod<sup>9</sup> and NSTX.<sup>1</sup> Section VI presents preliminary simulations for helicon launch in DIII-D,<sup>3</sup> and Section VII summarizes the results. The AORSA code is used as the tool to understand these issues, but the results are applicable to any simulation that uses the quasi-local approximation.

## II. EVIDENCE FOR NUMERICAL POLLUTION WHEN $k_{\parallel}$ APPROACHES ZERO

Since its inception in the early 2000s, the all-orders global wave solver AORSA<sup>8</sup> has exhibited noise in  $E_{\parallel}$ —the component of the radio frequency electric field parallel to the applied magnetic field. In the fast wave regime, this noise is minimal and does not interfere with the solution because  $E_{\parallel}$  is smaller than the perpendicular electric field by an electron to ion mass ratio. However, when slow waves are present in the solution, the noise in  $E_{\parallel}$  takes a particularly insidious form, appearing as an intricate short wavelength structure near the magnetic axis. When the resolution is increased, the amplitude of this structure increases until it eventually dominates the entire solution—a sign of numerical pollution.

Figure 1 shows an example of this pollution in a numerical solution for the wave electric field in the Alcator C-Mod tokamak.<sup>9</sup> A reduced frequency ( $f=30$  MHz) is used to simplify the problem by eliminating all ion resonances from the solution domain and leaving electron damping as the dominant loss mechanism. Only the shear Alfvén resonance remains on the high field (left) side of the plasma near  $R \approx 0.55$  m. A numerical grid of  $200 \times 200$  modes is used with warm electrons (1000 eV), cold ions (2 eV), and a toroidal mode number,  $n_{\varphi} = 12$ . In this example, a long wavelength, fast wave is excited by the antenna on the low field (right) side of the plasma near  $R \approx 0.9$  m. As it propagates across the plasma, the fast wave encounters the shear Alfvén resonance and is “mode-converted” to a shorter wavelength slow wave—the kinetic Alfvén wave (KAW)<sup>5</sup> near  $R \approx 0.55$  m in Fig. 1(a). The intricate short wavelength structure near the magnetic axis is due to numerical pollution. In Fig. 1(b), an approximate high harmonic dispersion solution<sup>10</sup> shows regions of propagation ( $k_{\perp}^2 > 0$ ) for the slow KAW (red) and for the fast wave (blue). Near the magnetic axis, there is a region of overlap where both fast and slow waves propagate simultaneously, and it is in this region that the numerical pollution appears.

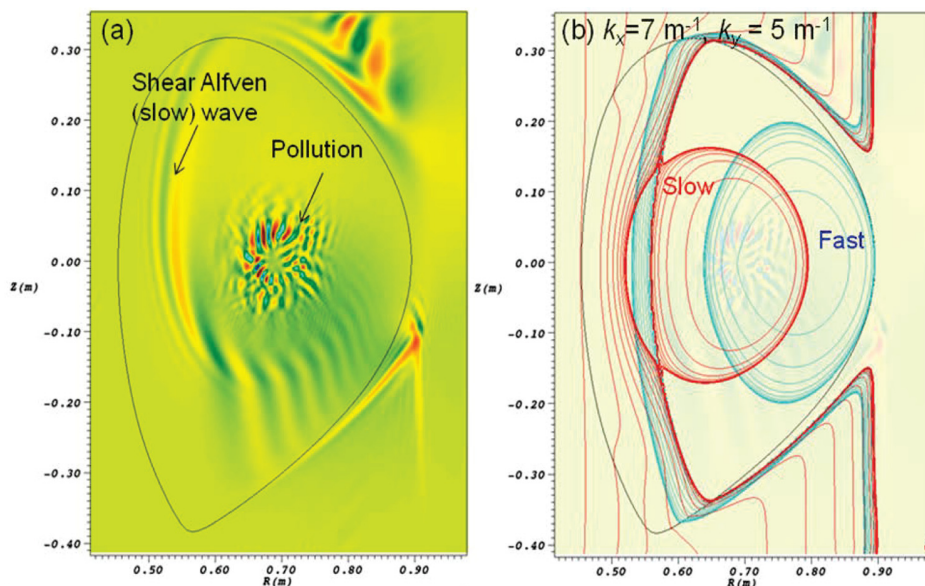


FIG. 1. (a) Real part of the perpendicular wave field,  $\text{Re}(E_x)$ , for  $f=30$  MHz in Alcator C-Mod: #1051206002. (b) The corresponding plasma dispersion solution<sup>10</sup> showing regions of fast wave propagation (blue) and slow wave propagation (red).

The appearance of short wavelength structures as in Fig. 1 requires two simultaneous conditions. First, there must be a slow wave branch ( $\omega/k_{\parallel} < v_{th,e}$ ) that excites high mode numbers in the AORSA spectrum ( $v_{th,e}$  is the electron thermal velocity). In addition,  $k_{\parallel}$  must be downshifted to very small values for these high mode numbers in the spectrum. Such a downshift is easily provided by the poloidal magnetic field in tokamak geometry. When  $k_{\parallel}$  for a particular mode is downshifted to near zero, that mode becomes essentially un-damped and can grow to very large amplitude. Figure 2(a) shows contours of  $\text{Re}(E_z)$  and lines along which  $k_{\parallel} = 0$  for two high mode numbers in the AORSA spectrum: (a)  $k_R = 700 \text{ m}^{-1}$ ,  $k_Z = 500 \text{ m}^{-1}$  and (b)  $k_R = 700 \text{ m}^{-1}$ ,  $k_Z = -500 \text{ m}^{-1}$ . Although only two modes are shown in Fig. 2, AORSA includes many such high mode numbers to represent the slow wave. All of these modes have different lines along which  $k_{\parallel} = 0$ , and all of these lines intersect the magnetic axis at different angles.

For cases involving slow waves, the very small values of  $k_{\parallel}$  along these lines can cause numerical pollution near the magnetic axis. Such small values of  $k_{\parallel}$  are not physically reasonable because they imply parallel wavelengths larger than the device-scale. There are many sources of broadening (in addition to thermal broadening) that could account for an effective minimum value of  $|k_{\parallel}|$ . For example, in the case of ion cyclotron resonance, parallel magnetic field gradients<sup>6</sup> provide such a mechanism. Often, however, solutions that display numerical pollution in  $E_{\parallel}$  contain no ion resonances—only the Alfvén resonance as in Figs. 1 and 2, or the electron Landau resonance. If we consider the effect of curved magnetic field lines in 3D geometry, a minimum average value of  $|k_{\parallel}|$  would be expected. In deriving the warm plasma conductivity, a local wave vector with straight magnetic field lines is assumed.<sup>5</sup> In this approximation, if  $|k_{\parallel}|$  is small at one point on the magnetic field line, it remains small at every point along the field line. This might be

reasonable near the outer edge of the tokamak where the field lines are relatively straight and pass many times around the torus before returning to the same poloidal position (e.g.,  $q = 5$ , where  $q$  is the safety factor or inverse rotational transform). However, near the magnetic axis where  $q = 1$ , a field line might pass only once around the torus before returning to the same poloidal location. In such cases, the field lines are effectively more “curved” than the outer field lines, and the straight field line assumption can easily be violated. If the value of  $|k_{\parallel}|$  along a field line is monitored near the  $q = 1$  surface, its magnitude is up-shifted near the top of the torus and downshifted near the bottom (or vice-versa depending on the sign of the poloidal field). In either case, it does not remain at one value (e.g., zero) for a long time, and it should have a non-zero average ( $\sim n_{\phi}/R$ ) after one pass around the torus. For basis sets using flux coordinates,<sup>7</sup> the straight field line approximation is more accurate because  $k_{\parallel}$  has relatively less variation along the flux coordinates than for the Cartesian coordinates used in AORSA.

These observations have motivated some “first principles” modifications to AORSA that include broadening of  $k_{\parallel}$  due to motion of electrons along the curved magnetic field lines in 3D toroidal geometry. Two methods for doing this are explored. First, the AORSA basis functions are Fourier expanded along the field line by tracing field line orbits numerically and evaluating the electron conductivity for each  $k_{\parallel}$  in the spectrum. The plasma current is then evaluated as a sum over this spectrum. Alternately, the phase of the basis function can be Taylor expanded along the magnetic field line about the point where the solution is calculated. Although this is only an approximation, it allows the parallel velocity integral in the plasma dispersion function<sup>11</sup> to be evaluated analytically. When the remaining time integral is calculated numerically, a new semi-analytic Z function emerges in the form of a two-dimensional table. This method is much faster than the more rigorous method of tracing field line orbits and is also more robust numerically.

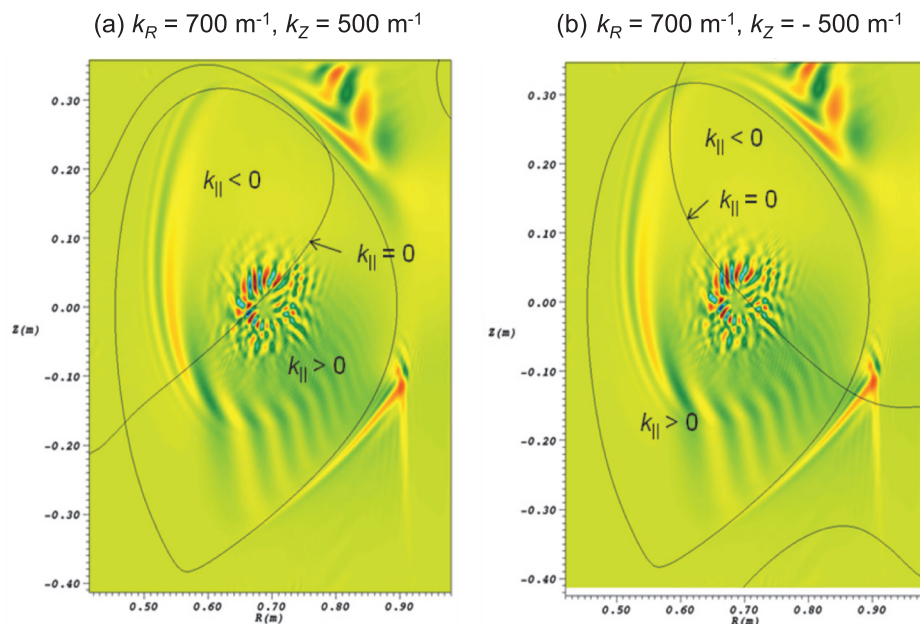


FIG. 2. (a) Contours of  $\text{Re}(E_z)$  with lines along which  $k_{\parallel} = 0$  for two high mode numbers in the AORSA spectrum: (a)  $k_R = 700 \text{ m}^{-1}$ ,  $k_Z = 500 \text{ m}^{-1}$  and (b)  $k_R = 700 \text{ m}^{-1}$ ,  $k_Z = -500 \text{ m}^{-1}$ .

### III. FOURIER EXPANSION OF THE AORSA BASIS SET ALONG A MAGNETIC FIELD LINE

For each  $k_R$  and  $k_Z$  in the AORSA spectrum, the Fourier basis function,  $E(l)$ , can be evaluated as a function of the magnetic field line length,  $l$

$$E(l) = e^{i[k_R R(l) + k_Z Z(l) + n_\phi \phi(l)]} = e^{i\Psi(l)}, \quad (1)$$

where the quantity in the square bracket will be called the “phase function”  $\Psi(l)$

$$\Psi(l) = k_R R(l) + k_Z Z(l) + n_\phi \phi(l). \quad (2)$$

The basis function in Eq. (1) can be evaluated over field line length  $l$  from  $-q \pi R_0$  to  $q \pi R_0$ , for a total field line length of  $L_{max} = 2\pi R_0 q$  where  $R_0$  is the major radius of the tokamak. The safety factor  $q$  is taken from the  $q$  profile for the equilibrium and is included to insure a complete revolution in the poloidal direction, although for some regions, e.g., outside of the last closed flux surface, a longer length is required. The field line coordinates,  $R(l)$ ,  $Z(l)$ , and  $\phi(l)$ , in Eq. (2) can be found by tracing field line orbits numerically. The basis function  $E(l)$  is then Fourier expanded along the field line to find its spectrum in  $k_{||}$

$$E(l) = \sum_n E_n e^{ik_{||,n} l}. \quad (3)$$

The number of modes in this summation is typically chosen between  $n = 256$  and  $n = 512$  depending on the particular problem and must be sufficient to resolve the maximum local (up-shifted) parallel wave vector which is several times  $q n_\phi / R$ . The electron conductivity  $\sigma$  can be evaluated for each  $k_{||,n}$  in the spectrum, and the parallel electron current is calculated as

$$J_e(l) = \sum_n \sigma_{3,3}^e(k_{||,n}) E_n e^{ik_{||,n} l}. \quad (4)$$

To save computational work, only the 3,3 (parallel) component of the electron conductivity tensor is included because it is the component that contributes most directly to electron Landau damping. Likewise, we include only the 0th harmonic in  $\sigma_{3,3}^e$  for electrons. Finally, an effective electron conductivity is calculated by dividing Eq. (4) by Eq. (3) and evaluating at the position along the field line where the solution is calculated,  $l = 0$ ,

$$\sigma_{3,3}^{e, \text{effective}}(0) = \frac{J(0)}{E(0)}. \quad (5)$$

This “effective” conductivity includes the variation of  $k_{||}$  due to curvature along the field line and can be used to replace the usual 0th harmonic term in the sum over harmonics for the parallel electron conductivity  $\sigma_{3,3}^e$ . For parameters where transit-time magnetic pumping is important, the elements of the conductivity tensor that couple perpendicular fields to parallel currents should be calculated using the same approach.

The method described above, while rigorous (with the assumption of constant parallel velocity), is extremely time consuming because of the large number of numerical field

line orbits required. In addition, there are two adjustable parameters: the field line length  $L_{max}$  and the number of modes in the Fourier expansion along the field line, and these must be adjusted for each particular problem. Therefore, it is desirable to find an alternate method that is both computationally faster and more robust numerically.

### IV. TAYLOR EXPANSION OF THE AORSA BASIS SET ALONG A MAGNETIC FIELD LINE

To save time computationally, the phase function  $\Psi(l)$  in Eq. (1) can be Taylor expanded about the position on the field line where the solution is calculated, i.e.,  $l = 0$

$$\Psi(l) = \Psi(0) + \frac{d\Psi}{dl} l + \frac{1}{2} \frac{d^2\Psi}{dl^2} l^2, \quad (6)$$

where

$$\frac{d\Psi}{dl} = k_R \frac{dR}{dl} + k_Z \frac{dZ}{dl} + n_\phi \frac{d\phi}{dl}. \quad (7)$$

The derivatives of the field line coordinates in Eq. (7) are given by the “equations of motion” of the field line:  $dR/dl = b_R$ ,  $dZ/dl = b_Z$ , and  $d\phi/dl = b_\phi/R$ , where  $b_R$ ,  $b_Z$ , and  $b_\phi$  are the normalized magnetic field components. Using this and the definition of  $k_{||}$

$$k_{||} = k_R b_R + k_Z b_Z + \frac{n_\phi}{R} b_\phi. \quad (8)$$

Eq. (6) becomes

$$\Psi(l) = \Psi(0) + k_{||} l + \frac{1}{2} \frac{dk_{||}}{dl} l^2 = \Psi(0) + k_{||} v_{||} \tau + \frac{1}{2} \frac{dk_{||}}{dl} v_{||}^2 \tau^2, \quad (9)$$

where  $l$  has been replaced by the product of the parallel velocity  $v_{||}$  and time  $\tau$ . We now see that the linear term in the Taylor expansion is equivalent to the local approximation, while the quadratic term is proportional to the physical parameter  $dk_{||}/dl$  which describes the rate of change of  $k_{||}$  along the field line. The quadratic term can also be described as the modification to the phase that results from field line curvature.<sup>6</sup> Equation (9) gives a phase function  $\Psi(\tau)$  that can be substituted directly into the integral expression for the plasma dispersion functions<sup>5,11</sup>

$$\begin{aligned} Z^{(0)} &= \frac{k_{||} i}{\sqrt{\pi}} \int_{-\infty}^{\infty} dv_{||} e^{-v_{||}^2/\alpha^2} \int_0^{\infty} d\tau e^{i\Psi(\tau) - i\omega\tau} \\ Z^{(1)} &= \frac{k_{||} i}{\alpha\sqrt{\pi}} \int_{-\infty}^{\infty} v_{||} dv_{||} e^{-v_{||}^2/\alpha^2} \int_0^{\infty} d\tau e^{i\Psi(\tau) - i\omega\tau} \\ Z^{(2)} &= \frac{k_{||} i}{\alpha^2\sqrt{\pi}} \int_{-\infty}^{\infty} v_{||}^2 dv_{||} e^{-v_{||}^2/\alpha^2} \int_0^{\infty} d\tau e^{i\Psi(\tau) - i\omega\tau}. \end{aligned} \quad (10)$$

Because the phase function in Eq. (10) is of order  $v_{||}^2$ , the integral over parallel velocity can be evaluated analytically<sup>12</sup> and the remaining integral over  $\tau$  can be done numerically (see Appendix A). The result can be expressed as a semi-analytic 2D function of the usual argument,  $\zeta = \omega/k_{||} v_{th}$ , and the additional physical parameter  $dK/dL = (\alpha/\omega)^2 dk_{||}/dl$  ( $\sim$  the rate of

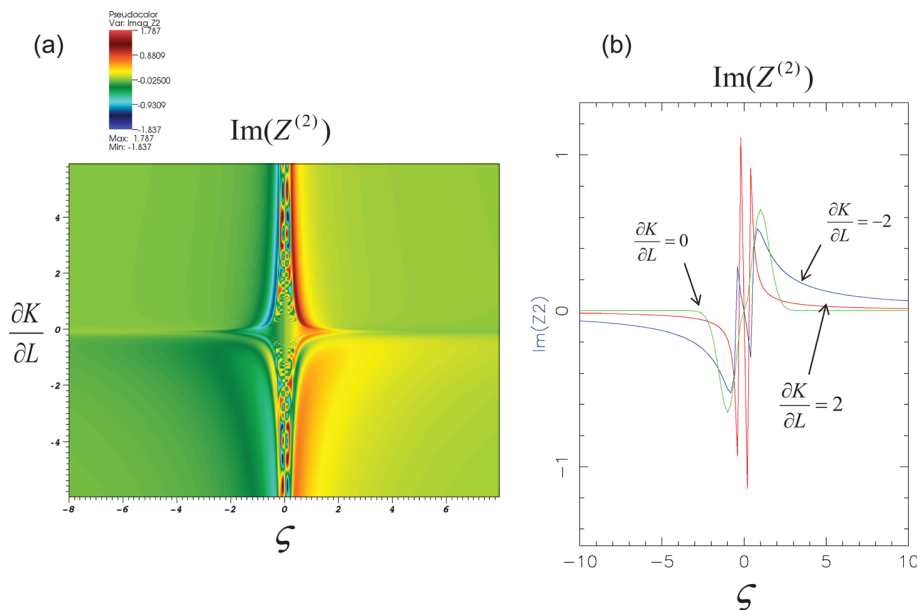


FIG. 3. (a) The imaginary part of the generalized plasma dispersion function  $\text{Im}(Z^{(2)})$  as a function of the conventional argument  $\zeta = \omega/k_{\parallel} \alpha$  (horizontal axis), and the rate of change of  $k_{\parallel}$  along a field line,  $dK/dl$  (vertical axis); (b) values of  $\text{Im}(Z^{(2)})$  along cuts through the data in (a) for  $dK/dL = 0$  (green),  $dK/dL = 2$  (red), and  $dK/dL = -2$  (blue).

change of  $k_{\parallel}$  along a field line). In Figure 3(a), the imaginary part of the generalized plasma dispersion function  $\text{Im}(Z^{(2)})$  is plotted as a function of the conventional argument  $\zeta = \omega/k_{\parallel} \alpha$  (horizontal axis), and the rate of change of  $k_{\parallel}$  along a field line,  $dK/dl$  (vertical axis). The imaginary part of  $Z^{(2)}$  is chosen for this figure because it is proportional to electron Landau damping which is the primary damping mechanism for the cases considered in this paper—see the last term in Eq. (B11) of Appendix B. In Fig. 3(b), the colored lines show cuts through the data of Fig. 3(a) at three different values of  $dK/dL$ . When  $dK/dL = 0$  (green), the new plasma dispersion function reduces to the conventional  $Z$  function, which rapidly decays to zero

for large  $\zeta$  (small  $k_{\parallel}$ ). However, when  $dK/dL \neq 0$  (red and blue lines), the new  $Z$  function remains significantly larger than the conventional  $Z$  function for large  $\zeta$ . Thus, when  $dK/dL$  is finite, the damping also remains finite even as  $k_{\parallel}$  approaches zero. The effect of negative  $dK/dL$  is stronger in this regard than positive  $dK/dL$  as can be seen from the expression for the new  $Z$  function in Eq. (A6) of Appendix A. When  $dK/dL$  is negative, the expression inside the radical remains positive, so  $\beta$  is smaller, and the finite value of  $dK/dL$  has a greater effect on  $Z^{(2)}$ .

The traditional method for calculating power absorption,  $\partial W/\partial t$ , in AORSA assumes that only the dissipative part of

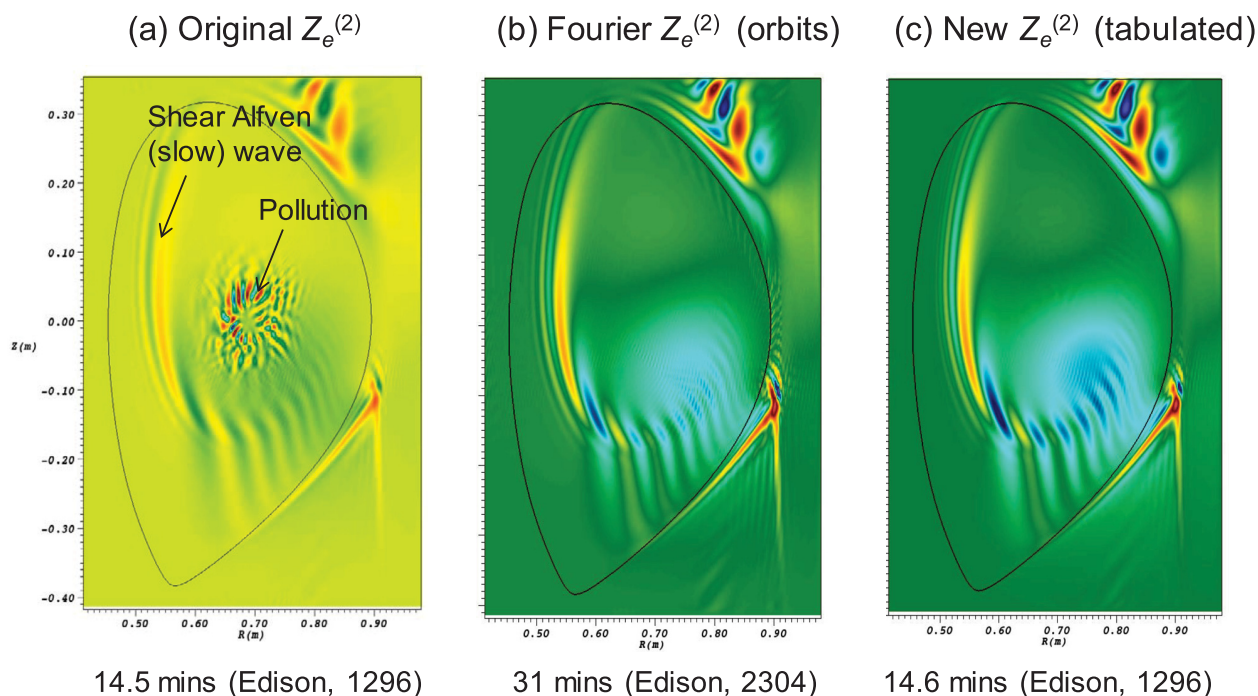


FIG. 4. Real part of the perpendicular wave field  $\text{Re}(E_z)$ , for three implementations of the electron  $Z$  function for the example of Fig. 1: (a) the original  $Z_e^{(2)}$ , (b) the Fourier-orbit  $Z_e^{(2)}$  with 256 modes and  $L_{\text{max}} = 2 \pi R_0 q$ , and (c) the new tabulated  $Z_e^{(2)}$ .

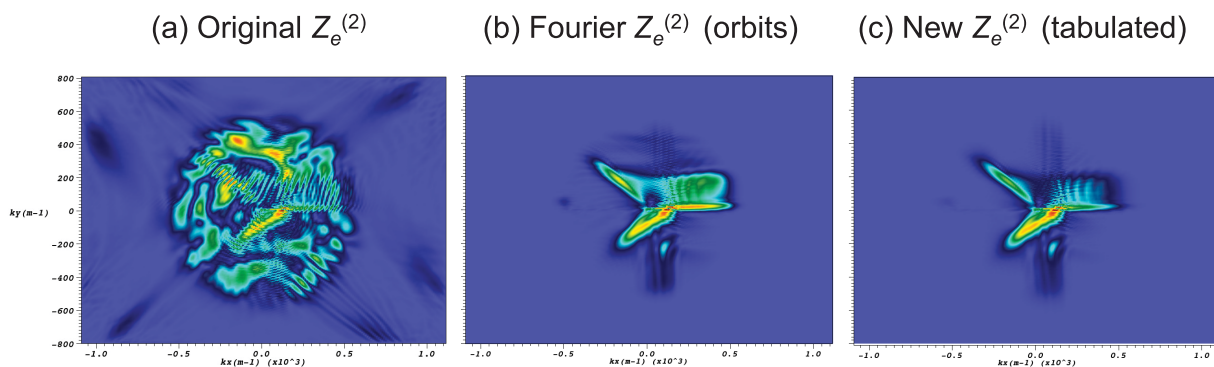


FIG. 5. Spectrum of modes that sum to give the wave field,  $\text{Re}(E_x)$ , for the solutions in Fig. 4.

the resonant integral contributes to power absorption and is therefore NOT consistent with the modified plasma dispersion function which contains both dissipative and non-dissipative parts. To recover consistency,  $\partial W/\partial t$  is reformulated in Appendix B, beginning with Eq. (9) in Ref. 12.

### V. FAST AND SLOW WAVE SIMULATIONS IN C-MOD AND NSTX

In this section, we repeat the calculation of Fig. 1 but with three different implementations of the electron Z function. In Fig. 4(a), the original Z function is used as in Fig. 1, and the wave field shows pollution near the magnetic axis. In Fig. 4(b), the rigorous Fourier expansion of Sec. III is used with 256 modes in the Fourier expansion along a field line of length  $L_{\text{max}} = 2 \pi R_0 q$ . In this case, the numerical pollution is totally eliminated, but the computation time is longer, even with the increased number of processors (2304 vs.

1296). In Fig. 4(c), the new tabulated Z function of Sec. IV is used. This method also eliminates the pollution, but the computation time is comparable to that with the simple Z function in Fig. 4(a). The slight differences between Figs. 4(b) and 4(c) are probably due to the choice of the two adjustable parameters in Fig. 4(b)—field line length,  $L_{\text{max}}$ , and number of modes along the field line.

Figure 5 shows the spectrum of modes that sum to give  $\text{Re}(E_x)$ , for the solutions in Fig. 4. As expected, the spectrum is poorly converged in Fig. 5(a) where pollution is present, but is well-converged in Figs. 5(b) and 5(c) where the pollution is absent. The “X” like pattern in Fig. 5(a) is indicative of the high mode numbers for which  $k_{\parallel}$  is down-shifted to small values. This happens when the values of  $k_R$  and  $k_Z$  are approximately equal and of opposite sign in Eq. (8), so that the first two terms partially cancel, leaving a relatively small value for  $k_{\parallel}$ .

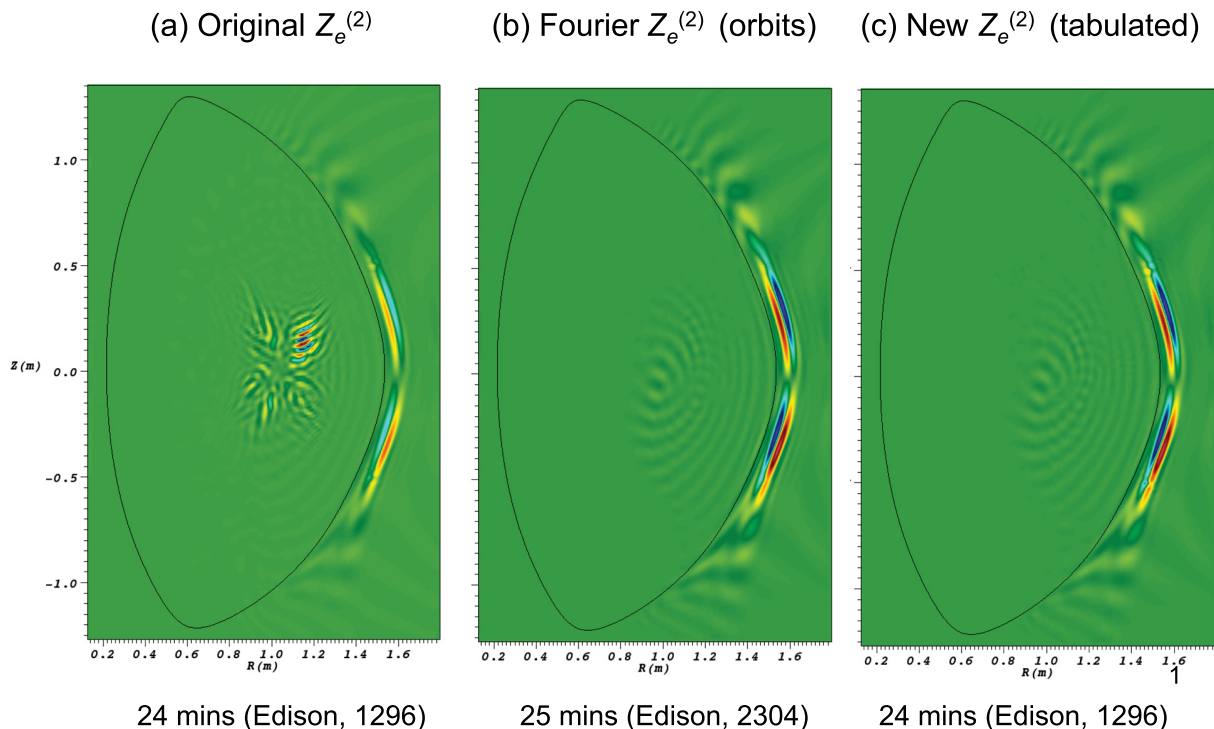


FIG. 6. Real part of the perpendicular wave for high harmonic fast wave heating in NSTX shot 123435 (Refs. 1 and 13): (a) original  $Z_e^{(2)}$ , (b) Fourier-orbit  $Z_e^{(2)}$  with  $L_{\text{max}} = 2 \pi R_0 q$  and 256 modes, and (c) new tabulated  $Z_e^{(2)}$ .

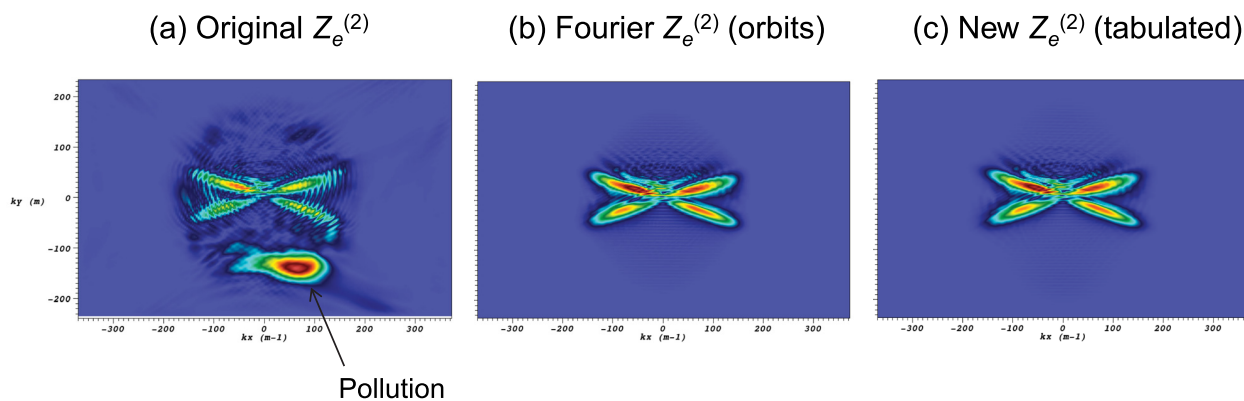


FIG. 7. Spectrum of modes that make up the solutions in Fig. 6.

Figures 6 and 7 show a similar example, but for high harmonic fast wave heating (HHFW) in NSTX.<sup>1</sup> This particular example (shot 123435) has been discussed in detail in Ref. 1. The implementation of the new  $Z$  function in Figs. 6(b) and 6(c) again eliminates the X-like pattern of pollution in Fig. 6(a). The amplitude of the pollution is largest in the upper right quadrant of Fig. 6(a), and corresponds to the high amplitude (red) peak in the spectrum of Fig. 7(a).

The new plasma dispersion function described above is intended to eliminate numerical pollution thereby allowing converged solutions with significant slow wave components. In Fig. 8, we show an example where both fast and slow waves are present simultaneously. The geometry of NSTX shot 112705 is used, but with the frequency reduced to 10 MHz to ensure that the wavelength of the slow wave is long enough to be resolved numerically using a  $400 \times 400$  grid. Using the complete Fourier expansion along field line orbits as described in Sec. II with  $L_{max} = 2 \pi R_0 q$ , 256 modes and  $k_{||} = -127:128$ , we plot  $\text{Re}(E_x)$  in Fig. 8(a), where the fast wavelength is about  $\lambda \approx 10$  cm and corresponds to a wave number,  $k = 2 \pi / \lambda \approx 62 \text{ m}^{-1}$ . The slow wave is visible as a slight ripple on the fast wave in the blowup of Fig. 8(b) and has a wavelength of about  $\lambda \approx 2$  cm with a corresponding

wave number,  $k \approx 300 \text{ m}^{-1}$ . These are in approximate agreement with the simplified high harmonic dispersion solution<sup>10</sup> shown in Fig. 9, where red denotes the slow wave branch, and blue denotes the fast wave branch. Positive and negative values represent the right- and left-going waves, respectively.

## VI. HELICON WAVE SIMULATIONS IN DIII-D

Helicon waves (also called “whistlers,” or “very high harmonic fast waves,” or “lower hybrid fast waves”) can be effective for driving off-axis currents in tokamaks.<sup>3</sup> Fast waves in the frequency range 500 to 1500 MHz tend to propagate in a spiral around the magnetic axis. These frequencies are well above the ion cyclotron frequency ( $\sim 30$ th harmonic), but below the lower hybrid frequency. For high electron temperatures and densities, these waves are absorbed in a single pass by electron Landau damping and can drive off-axis currents. Simulation of this process with a full-wave model such as AORSA is difficult because of the very large number of modes required to resolve the short wavelengths, and because of the high ion harmonic resonances involved. Fig. 10 shows the magnitude of the total wave electric field for a simulation using the complete

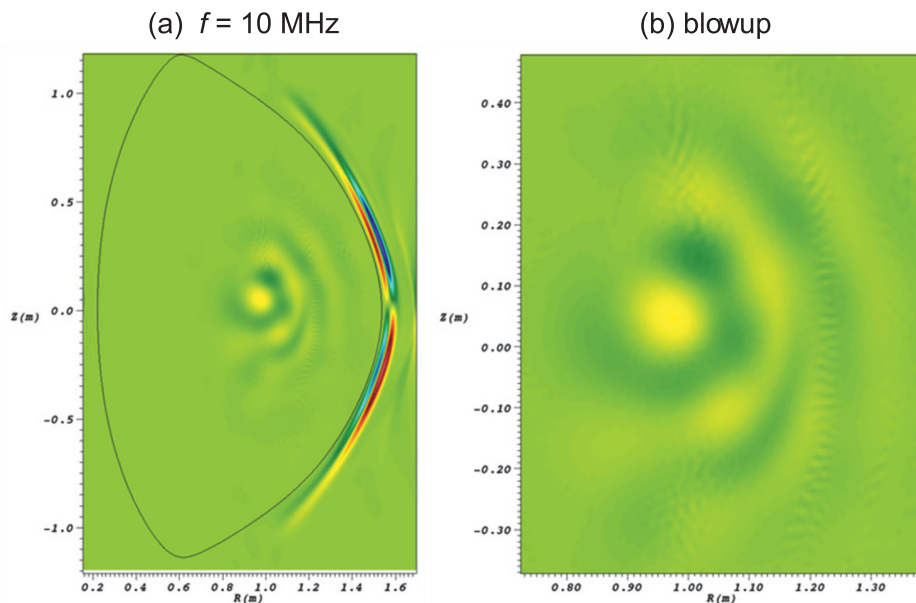


FIG. 8. (a)  $\text{Re}(E_x)$  for NSTX shot 112705 with  $f = 10$  MHz using the complete Fourier expansion along numerical field line orbits as described in Sec. II with  $L_{max} = 2 \pi R_0 q$  and 256 modes; (b) blow-up of the result in (a).

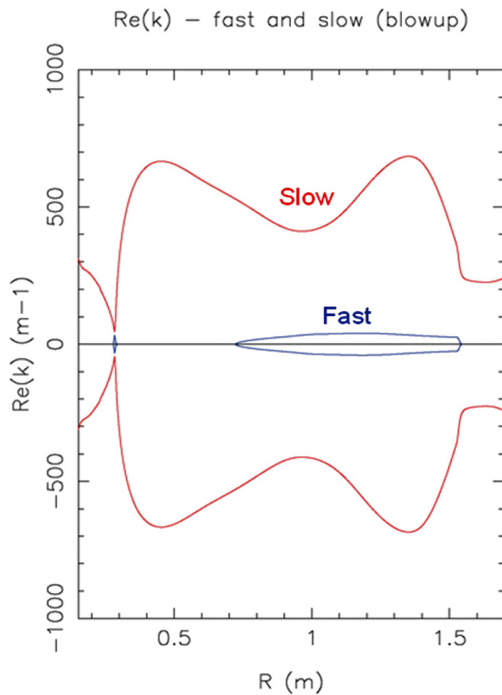


FIG. 9. Approximate high harmonic dispersion solution<sup>10</sup> for the wave solution in Fig. 8.

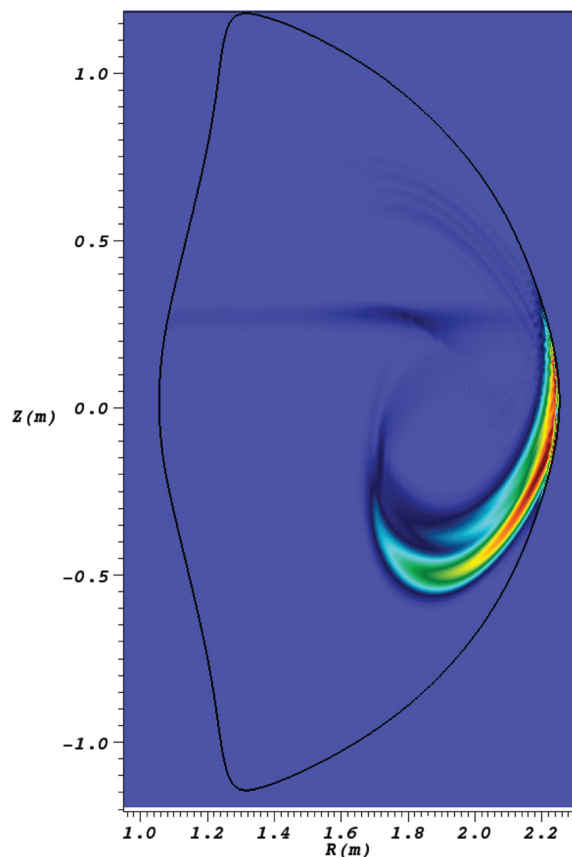


FIG. 10. Magnitude of the total wave electric field for a helicon wave solution using the complete Fourier expansion technique described in Sec. II with 512 Fourier modes along the field line.

Fourier expansion along the field line orbits, as described in Sec. II. The magnetic equilibrium and plasma profiles correspond to an advanced tokamak scenario in DIII-D:<sup>14</sup>  $f=500$  MHz,  $B_0=1.49$  T,  $n_\phi=-71$ ,  $n_{||}=-3.0$ , with electron power absorbed = 1.77 MW. Ion resonances of up to 50th harmonic are included in the solution with a numerical grid of  $500 \times 320$  modes. Because helicon waves propagate primarily toroidally, many Fourier modes are required to resolve the variation of the helicon wave along the magnetic field line. This is evident in Fig. 10 where 512 Fourier modes are needed to get the correct converged solution which shows the typical spiral-like propagation pattern.

In Fig. 10, the plasma edge, or “scrape-off layer” (SOL) has been omitted from the solution domain, and replaced with a metal wall boundary condition at the last closed flux surface ( $\rho=1$ ). Although the SOL is neglected in this simulation, it could play an important role if a substantial amount of power is coupled to slow waves in the SOL. An approximate high harmonic dispersion relation<sup>10</sup> shows that slow waves do in fact propagate easily in the edge plasma region with very small wavelengths near the lower hybrid resonance at  $\rho=1$ . Converged helicon solutions including the SOL will be left for a future paper.

## VII. SUMMARY

In this paper, we have taken the first steps toward accurate modeling of slow waves with the all-orders global wave solver, AORSA. Previous simulations exhibit numerical pollution in  $E_{||}$  when slow waves are present. The source of this pollution appears to be high mode numbers in the spectrum for which  $k_{||}$  is downshifted to near zero. To eliminate this pollution and allow accurate solutions containing significant slow wave components, a generalized semi-analytic plasma dispersion function ( $Z$ ) has been developed for electrons to take into account broadening of  $k_{||}$  due to motion along the curved magnetic field lines. This new  $Z$  function eliminates numerical pollution and allows converged solutions when both fast and slow waves are present simultaneously. A more rigorous treatment involves a complete Fourier expansion of the AORSA basis set along the field lines by tracing a large number of field line orbits numerically. For most cases, this more rigorous treatment gives approximately the same result as the semi-analytic  $Z$  function, but with a higher computational cost.

## ACKNOWLEDGMENTS

This work was sponsored by Scientific Discovery through Advanced Computing (SciDAC) and the Oak Ridge National Laboratory, managed by UT-Battelle, LLC, for the U.S. Department of Energy under Contract No. DE-AC-5-00OR22725. Numerical calculations used resources of the National Energy Research Scientific Computing Center, a DOE Office of Science User Facility supported by the Office of Science of the U.S. Department of Energy under Contract No. DE-AC02-05CH11231.

## APPENDIX A—CALCULATION OF THE GENERALIZED Z FUNCTION

In this Appendix, we carry out the velocity space integrals in Eq. (10) to express the generalized Z function as a semi-analytic 2D function of the usual argument,  $\zeta = \omega/k_{\parallel}$ ,  $v_{th}$ , and an additional physical parameter proportional to the rate of change of  $k_{\parallel}$  along a field line. Substituting Eq. (9) for the phase function  $\Psi(l)$  into Eq. (10) gives for  $Z^{(2)}$

$$Z_l^{(2)} = \frac{k_{\parallel} i \alpha}{\sqrt{\pi}} \int_{-\infty}^{\infty} u^2 du e^{-u^2} \int_{-\infty}^{\infty} d\tau e^{i[k_{\parallel} \alpha \tau + \frac{1}{2} \frac{dk_{\parallel}}{dl} \alpha^2 \tau^2] - i \omega \tau}, \quad (\text{A1})$$

where we have defined the non-dimensional velocity  $u = v_{\parallel}/\alpha$ . Reversing the order of integration and defining

$$\beta = \frac{1}{\sqrt{1 - \frac{i}{2} \frac{dk_{\parallel}}{dl} \alpha^2 \tau^2}}. \quad (\text{A2})$$

Eq. (A1) becomes

$$Z_l^{(2)} = \frac{k_{\parallel} i \alpha}{\sqrt{\pi}} \int_{-\infty}^{\infty} d\tau e^{-i \omega \tau} \int_{-\infty}^{\infty} u^2 du e^{-\left(\frac{u^2}{\beta^2} - i k_{\parallel} \alpha \tau\right)}. \quad (\text{A3})$$

Completing the square in the exponent gives

$$\left(\frac{u}{\beta} - \frac{i}{2} k_{\parallel} \alpha \tau \beta\right)^2 = \frac{u^2}{\beta^2} - i u k_{\parallel} \alpha \tau - \frac{1}{4} k_{\parallel}^2 \alpha^2 \tau^2 \beta^2, \quad (\text{A4})$$

so that (A3) becomes

$$Z_l^{(2)} = \frac{|k_{\parallel}| i \alpha}{\sqrt{\pi}} \int_{-\infty}^{\infty} d\tau e^{-i \omega \tau} \int_{-\infty}^{\infty} u^2 du e^{-\left(\frac{u^2}{\beta^2} - \frac{i}{2} k_{\parallel} \alpha \tau \beta\right)^2 - \frac{1}{4} k_{\parallel}^2 \alpha^2 \tau^2 \beta^2}. \quad (\text{A5})$$

The integral over velocity  $u$  can be done analytically by changing variables from  $u$  to  $w = \frac{u}{\beta} - \frac{i}{2} k_{\parallel} \alpha \tau \beta$  in which case Eq. (A5) reduces to

$$Z^{(2)} = \frac{i}{2} \int_0^{\infty} \frac{\beta^3}{\zeta} dz \left(1 - \frac{1}{2} \frac{z^2 \beta^2}{\zeta^2}\right) e^{iz - \frac{1}{4} \left(\frac{z\beta}{\zeta}\right)^2}, \quad (\text{A6})$$

where  $z = -\omega \tau$ ,  $\zeta = \omega/k_{\parallel} \alpha$ , and

$$\beta = \frac{1}{\sqrt{1 - \frac{i}{2} \frac{dK}{dL} z^2}}, \quad (\text{A7})$$

with  $dK/dL = (\alpha/\omega)^2 dk_{\parallel}/dl$ . Repeating the same steps for  $Z^{(0)}$  and  $Z^{(1)}$  gives

$$Z^{(0)} = i \int_0^{\infty} \frac{\beta}{\zeta} dz e^{iz - \frac{1}{4} \left(\frac{z\beta}{\zeta}\right)^2}, \quad (\text{A8})$$

$$Z^{(1)} = \frac{1}{2} \int_0^{\infty} \frac{\beta^3}{\zeta^2} z dz e^{iz - \frac{1}{4} \left(\frac{z\beta}{\zeta}\right)^2}. \quad (\text{A9})$$

To recover the usual forms for  $Z^{(0)}$ ,  $Z^{(1)}$ , and  $Z^{(2)}$  given by Stix<sup>5</sup> and Smithe,<sup>6</sup> we set  $dK/dL = 0$  in (A7), so that  $\beta = 1$ , and changing the variable of integration from  $z$  to  $x = z/\zeta$  gives

$$\begin{aligned} Z^{(0)} &= i \int_0^{\infty \text{sgn} k_{\parallel}} dx e^{i \zeta x - \frac{1}{4} x^2}, \\ Z^{(1)} &= \frac{1}{2} \int_0^{\infty \text{sgn} k_{\parallel}} x dx e^{i \zeta x - \frac{1}{4} x^2}, \\ Z^{(2)} &= \frac{i}{2} \int_0^{\infty \text{sgn} k_{\parallel}} dx \left(1 - \frac{1}{2} x^2\right) e^{i \zeta x - \frac{1}{4} x^2}. \end{aligned} \quad (\text{A10})$$

Note that the sign of  $k_{\parallel}$  now appears explicitly in the limit of integration. However, the general result in Eqs. (A6), (A8), and (A9) includes the sign of  $k_{\parallel}$  automatically through the sign of  $\zeta$  without requiring that it be specified independently in limit of integration. Therefore, we do not require two separate tables for positive and negative  $k_{\parallel}$  when calculating the generalized Z function—one table is sufficient.

## APPENDIX B—REFORMULATION OF $\partial W/\partial t$ FOR THE MODIFIED Z FUNCTION

The traditional method for calculating  $\partial W/\partial t$  in AORSA assumes that only the dissipative part of the resonant integral contributes to power absorption. This is NOT consistent with the modified plasma dispersion function derived in this paper, which includes both dissipative and non-dissipative parts. To achieve consistency,  $\partial W/\partial t$  has been reformulated starting with Eq. (9) of Ref. 15

$$P_{RF} = \frac{1}{2} \text{Re} \left\{ \frac{\varepsilon_0 \omega}{i} \sum_{\mathbf{k}_1, \mathbf{k}_2} e^{i(\mathbf{k}_1 - \mathbf{k}_2) \cdot \mathbf{r}} \mathbf{E}_{\mathbf{k}_2}^* \cdot \mathbf{W}_l \cdot \mathbf{E}_{\mathbf{k}_1} \right\}, \quad (\text{B1})$$

where  $\mathbf{W}_l$  is the local energy absorption kernel defined in Eq. (12) of Ref. 15

$$\begin{aligned} \mathbf{W}_l &= -\frac{\omega_p^2}{\omega} \sum_{l=-\infty}^{\infty} e^{il(\beta_1 - \beta_2)} \mathbf{C}^{-1}(\beta_2) \\ &\cdot \left[ i \int_{-\infty}^{\infty} d\tau \int_0^{\infty} d^3 v e^{i(\omega - l\Omega - k_{\parallel} v_{\parallel}) \tau} \frac{1}{2} \mathbf{a}_l^T \mathbf{b}_l \right] \cdot \mathbf{C}(\beta_1). \end{aligned} \quad (\text{B2})$$

$\mathbf{C}(\beta)$  is the rotation matrix that transforms the electric field from local magnetic coordinates to the  $(E_+, E_-, E_{\parallel})$  frame with  $k_{\beta} = 0$

$$\mathbf{C}(\beta) = \begin{pmatrix} e^{i\beta} & -ie^{i\beta} & 0 \\ e^{-i\beta} & -ie^{-i\beta} & 0 \\ 0 & 0 & \sqrt{2} \end{pmatrix}. \quad (\text{B3})$$

The angle between  $k_{\perp}$  and  $k_x$  is defined as  $\beta$  such that  $\cos \beta = k_x/k_{\perp}$  and  $\sin \beta = k_y/k_{\perp}$ . In the dyadic tensor in Eq. (B2),  $\mathbf{a}_l = (v_{\perp} J_{l+1}(\xi), v_{\perp} J_{l-1}(\xi), \sqrt{2} v_{\parallel} J_l(\xi))$ , where the argument of the Bessel functions is  $\xi = k_{\perp} v_{\perp} / \Omega$ . Restricting application to Maxwellian distributions,  $\mathbf{b}_l = -\frac{2f_0}{z^2} \mathbf{a}_l$ , where  $\alpha$  is the thermal velocity of the Maxwellian. To simplify the notation, we define  $\boldsymbol{\varepsilon}$  to be the rotated electric field vector,  $\boldsymbol{\varepsilon}_{\mathbf{k}} = \mathbf{C}(\beta) \cdot \mathbf{E}_{\mathbf{k}} e^{i(\mathbf{k} \cdot \mathbf{r} + l\beta)}$ , and Eq. (B1) becomes

$$\begin{aligned} P_{RF} &= -\frac{\pi \omega_p^2 \varepsilon_0}{2} \text{Re} \left\{ \sum_{\mathbf{k}_1, \mathbf{k}_2} \boldsymbol{\varepsilon}_{\mathbf{k}_2}^* \cdot \sum_{l=-\infty}^{\infty} \left[ \int_{-\infty}^{\infty} d\tau \right. \right. \\ &\left. \left. \times \int_0^{\infty} v_{\perp} dv_{\perp} dv_{\parallel} e^{i\psi_l \tau} \mathbf{a}_l^T \mathbf{b}_l \right] \cdot \boldsymbol{\varepsilon}_{\mathbf{k}_1} \right\}, \end{aligned} \quad (\text{B4})$$

where  $\psi_l = \omega - l\Omega - k_{\parallel}v_{\parallel}$  is the ‘‘phase function.’’ For electrons,  $l=0$  so that  $\psi_l = \omega - k_{\parallel}v_{\parallel}$ . Note that  $\psi_l = \omega - \Psi/\tau$ , where  $\Psi$  is defined in Eq. (2).

The algebraic goal is to move the perpendicular velocity integral in Eq. (B4) outside of the multiple sums, in which case the 4D sum over  $k$ 's can be written as the product of two 2D sums.<sup>16</sup> The parallel velocity integral remains on the inside and can be evaluated as an analytic or tabulated  $Z$  function. The perpendicular velocity integral remains on the outside and is evaluated numerically. The phase of the integrand  $\psi_l = \omega - l\Omega - k_{\parallel}v_{\parallel}$  is left in a general form to be consistent with the modified  $Z$  function. The perpendicular and parallel velocity integrals can be separated by defining  $\mathbf{a}_l = v_{\perp}\mathbf{a}_l^{\perp} + v_{\parallel}\mathbf{a}_l^{\parallel}$  and  $\mathbf{b}_l = -\frac{2f_0^{\perp}f_0^{\parallel}}{\alpha^2}(v_{\perp}\mathbf{b}_l^{\perp} + v_{\parallel}\mathbf{b}_l^{\parallel})$ , where  $f_0^{\perp} = \frac{n_0}{\pi^{3/2}\alpha^3}e^{-v_{\perp}^2/\alpha^2}$  and  $f_0^{\parallel} = e^{-v_{\parallel}^2/\alpha^2}$  with

$$\begin{aligned}\mathbf{a}_l^{\perp} &= \mathbf{b}_l^{\perp} = (J_{l+1}(\xi), J_{l-1}(\xi), 0) \\ \mathbf{a}_l^{\parallel} &= \mathbf{b}_l^{\parallel} = (0, 0, \sqrt{2}J_l(\xi)).\end{aligned}\quad (\text{B5})$$

Then, Eq. (B4) becomes

$$P_{RF} = -\frac{\pi\omega_p^2\varepsilon_0}{2}\text{Re}\sum_{l=-\infty}^{\infty}\int_0^{\infty}v_{\perp}dv_{\perp}\left\{\sum_{\mathbf{k}_1,\mathbf{k}_2}\boldsymbol{\varepsilon}_{\mathbf{k}_2}^*\cdot\left[\int_{-\infty}^{\infty}d\tau\int_0^{\infty}dv_{\parallel}e^{i\psi_l\tau}\mathbf{a}_l^T\mathbf{b}_l\right]\cdot\boldsymbol{\varepsilon}_{\mathbf{k}_1}\right\},\quad (\text{B6})$$

where

$$\begin{aligned}\mathbf{a}_l^T\mathbf{b}_l &= -\frac{2f_0^{\perp}f_0^{\parallel}}{\alpha^2}(v_{\perp}\mathbf{a}_l^{\perp} + v_{\parallel}\mathbf{a}_l^{\parallel})^T(v_{\perp}\mathbf{b}_l^{\perp} + v_{\parallel}\mathbf{b}_l^{\parallel}) \\ &= -\frac{2f_0^{\perp}f_0^{\parallel}}{\alpha^2}(v_{\perp}^2\mathbf{a}_l^{\perp,T}\mathbf{b}_l^{\perp} + v_{\perp}v_{\parallel}\mathbf{a}_l^{\perp,T}\mathbf{b}_l^{\parallel} + v_{\perp}v_{\parallel}\mathbf{a}_l^{\parallel,T}\mathbf{b}_l^{\perp} + v_{\parallel}^2\mathbf{a}_l^{\parallel,T}\mathbf{b}_l^{\parallel}),\end{aligned}\quad (\text{B7})$$

so that

$$\begin{aligned}P_{RF} &= \pi\omega_p^2\varepsilon_0\text{Re}\sum_{l=-\infty}^{\infty}\int_0^{\infty}v_{\perp}dv_{\perp}\frac{f_0^{\perp}}{\alpha^2}\sum_{\mathbf{k}_1,\mathbf{k}_2}\boldsymbol{\varepsilon}_{\mathbf{k}_2}^*\cdot\left\{v_{\perp}^2\int_{-\infty}^{\infty}d\tau\int_0^{\infty}dv_{\parallel}e^{i\psi_l\tau}e^{-v_{\parallel}^2/\alpha^2}\mathbf{a}_l^{\perp,T}\mathbf{b}_l^{\perp}\right. \\ &\quad + v_{\perp}\int_{-\infty}^{\infty}d\tau\int_0^{\infty}dv_{\parallel}e^{i\psi_l\tau}v_{\parallel}e^{-v_{\parallel}^2/\alpha^2}v_{\parallel}^2\mathbf{a}_l^{\perp,T}\mathbf{b}_l^{\parallel} + v_{\perp}\int_{-\infty}^{\infty}d\tau\int_0^{\infty}dv_{\parallel}e^{i\psi_l\tau}v_{\parallel}e^{-v_{\parallel}^2/\alpha^2}v_{\parallel}^2\mathbf{a}_l^{\parallel,T}\mathbf{b}_l^{\perp} \\ &\quad \left. + \int_{-\infty}^{\infty}d\tau\int_0^{\infty}dv_{\parallel}e^{i\psi_l\tau}e^{-v_{\parallel}^2/\alpha^2}v_{\parallel}^2\mathbf{a}_l^{\parallel,T}\mathbf{b}_l^{\parallel}\right\}\cdot\boldsymbol{\varepsilon}_{\mathbf{k}_1}.\end{aligned}\quad (\text{B8})$$

Defining the plasma dispersion functions as<sup>5</sup>

$$\begin{aligned}Z_l^{(2)} &= \frac{|k_{\parallel}|i}{\alpha^2\sqrt{\pi}}\int_{-\infty}^{\infty}v_{\parallel}^2dv_{\parallel}e^{-v_{\parallel}^2/\alpha^2}\int_0^{\infty}d\tau e^{i\psi_l\tau}, \\ Z_l^{(1)} &= \frac{|k_{\parallel}|i}{\alpha^2\sqrt{\pi}}\int_{-\infty}^{\infty}v_{\parallel}dv_{\parallel}e^{-v_{\parallel}^2/\alpha^2}\int_0^{\infty}d\tau e^{i\psi_l\tau}, \\ Z_l^{(0)} &= \frac{|k_{\parallel}|i}{\alpha^2\sqrt{\pi}}\int_{-\infty}^{\infty}dv_{\parallel}e^{-v_{\parallel}^2/\alpha^2}\int_0^{\infty}d\tau e^{i\psi_l\tau},\end{aligned}\quad (\text{B9})$$

Eq. (B8) can finally be written as the product of two sums

$$\begin{aligned}P_{RF} &= \pi\omega_p^2\varepsilon_0\text{Re}\sum_{l=-\infty}^{\infty}\int_0^{\infty}dv_{\perp}\frac{f_0^{\perp}}{\alpha^2}\left\{\sum_{k_2}[\boldsymbol{\varepsilon}_{\mathbf{k}_2}^*\cdot v_{\perp}^2\mathbf{a}_l^{\perp,T}]\sum_{k_1}\left[\mathbf{b}_l^{\perp}\cdot\frac{\sqrt{\pi}}{ik_{\parallel}}Z_l^{(0)}\boldsymbol{\varepsilon}_{\mathbf{k}_1}\right]\right. \\ &\quad + \sum_{k_2}[\boldsymbol{\varepsilon}_{\mathbf{k}_2}^*\cdot v_{\perp}^2\mathbf{a}_l^{\perp,T}]\sum_{k_1}\left[\mathbf{b}_l^{\parallel}\cdot\frac{\alpha\sqrt{\pi}}{ik_{\parallel}}Z_l^{(1)}\boldsymbol{\varepsilon}_{\mathbf{k}_1}\right] + \sum_{k_2}[\boldsymbol{\varepsilon}_{\mathbf{k}_2}^*\cdot v_{\perp}^2\mathbf{a}_l^{\parallel,T}]\sum_{k_1}\left[\mathbf{b}_l^{\perp}\cdot\frac{\alpha\sqrt{\pi}}{ik_{\parallel}}Z_l^{(1)}\boldsymbol{\varepsilon}_{\mathbf{k}_1}\right] \\ &\quad \left. + \sum_{k_2}[\boldsymbol{\varepsilon}_{\mathbf{k}_2}^*\cdot v_{\perp}\mathbf{a}_l^{\parallel,T}]\sum_{k_1}\left[\mathbf{b}_l^{\parallel}\cdot\frac{\alpha^2\sqrt{\pi}}{ik_{\parallel}}Z_l^{(2)}\boldsymbol{\varepsilon}_{\mathbf{k}_1}\right]\right\}.\end{aligned}\quad (\text{B10})$$

AORSA uses a non-dimensional system of units based on the CQL3D Fokker Planck code<sup>17</sup> in which the distribution function  $f$  is normalized to  $n/v_c^3$ , where  $n$  is the density, and the velocities  $u_{\perp}$  and  $u_{\parallel}$  are normalized to  $v_c = c/\sqrt{\mu}$ , where  $c$  is the speed of light,  $\mu = mc^2/2eE_{norm}$ , and  $E_{norm}$  is the maximum energy in eV at which the numerical distribution function is evaluated. Using these definitions, Eq. (B10) can be rewritten as

$$\begin{aligned}
P_{RF} = & \pi^{3/2} \frac{\omega_p^2 \epsilon_0}{\omega} \text{Im} \sum_{l=-\infty}^{\infty} \int_0^{\infty} \frac{\sqrt{\mu_0}}{u_0} du_{\perp} f_{CQL}^{\perp} \left\{ (u_{\perp} u_0)^3 \sum_{k_2} [\mathbf{e}_{\mathbf{k}_2}^* \cdot \mathbf{a}_l^{\perp, T}] \sum_{k_1} \left[ \mathbf{b}_l^{\perp} \cdot \frac{1}{n_{\parallel}} Z_l^{(0)} \mathbf{e}_{\mathbf{k}_1} \right] \right. \\
& + (u_{\perp} u_0)^2 \sum_{k_2} [\mathbf{e}_{\mathbf{k}_2}^* \cdot \mathbf{a}_l^{\perp, T}] \sum_{k_1} \left[ \mathbf{b}_l^{\parallel} \cdot \frac{1}{n_{\parallel}} Z_l^{(1)} \mathbf{e}_{\mathbf{k}_1} \right] \\
& + (u_{\perp} u_0)^2 \sum_{k_2} [\mathbf{e}_{\mathbf{k}_2}^* \cdot \mathbf{a}_l^{\parallel, T}] \sum_{k_1} \left[ \mathbf{b}_l^{\perp} \cdot \frac{1}{n_{\parallel}} Z_l^{(1)} \mathbf{e}_{\mathbf{k}_1} \right] \\
& \left. + (u_{\perp} u_0) \sum_{k_2} [\mathbf{e}_{\mathbf{k}_2}^* \cdot \mathbf{a}_l^{\parallel, T}] \sum_{k_1} \left[ \mathbf{b}_l^{\parallel} \cdot \frac{1}{n_{\parallel}} Z_l^{(2)} \mathbf{e}_{\mathbf{k}_1} \right] \right\} \quad (\text{LD}), \quad (\text{B11})
\end{aligned}$$

where  $u_0$  is  $u_0 = v_{\max}/\alpha = c/\alpha\sqrt{\mu}$ ,  $n_{\parallel} = k_{\parallel}c/\omega$ , and  $v_{\max}$  is the maximum velocity corresponding to  $E_{\text{norm}}$ , and  $f_{CQL}^{\perp} = \frac{u_0^3}{\pi^{3/2}} e^{-u_{\perp}^2 u_0^2}$ . Equation (B11) is the expression used in AORSA, with  $u_0 = 3$  for the assumed Maxwellian. The terms in Eq. (B11) are labeled with their corresponding physical heating mechanism, i.e., Landau damping (LD), transit time magnetic pumping (TTMP), and cross terms (X term).

Term 4 in Eq. (B11) can be checked by comparing to the usual expression for electron Landau damping.<sup>5</sup> Keeping only the  $l=0$  term in the sum over harmonics, and only the dissipative (imaginary) part of the  $Z$  function,  $Z_l^{(2)} = \sqrt{\pi} i \zeta^2 e^{-\zeta^2}$ , where  $\zeta = \omega/k_{\parallel}\alpha$ , and using  $\mathbf{a}_l^{\parallel} = \mathbf{b}_l^{\parallel} = (0, 0, \sqrt{2}J_l(\xi))$  with small  $\xi$ , term 4 reduces to

$$P_{RF} = \sqrt{\pi} \frac{\omega_p^2 \epsilon_0}{\omega} \zeta^3 e^{-\zeta^2} |E_{\parallel}|^2, \quad (\text{B12})$$

which agrees with the usual expression for electron Landau damping.<sup>5</sup>

<sup>1</sup>C. K. Phillips, R. E. Bell, L. A. Berry, P. T. Bonoli, R. W. Harvey, J. C. Hosea, E. F. Jaeger, B. P. LeBlanc, P. M. Ryan, G. Taylor, E. J. Valeo, J. B. Wilgen, J. R. Wilson, J. C. Wright, H. Yuhand, and the NSTX Team, *Nucl. Fusion* **49**, 075015 (2009).

<sup>2</sup>J. E. Menard, S. Gerhardt, M. Bell, J. Bialek, A. Brooks, J. Canik, J. Chrzanowski, M. Denault, L. Dudek, and D. A. Gates, *Nucl. Fusion* **52**, 083015 (2012).

<sup>3</sup>R. Prater, C. P. Moeller, R. I. Pinsker, M. Porkolab, O. Meneghini, and V. L. Vdovin, *Nucl. Fusion* **54**, 083024 (2014).

<sup>4</sup>R. V. Budny, L. Berry, R. Bilato, P. Bonoli, M. Brambilla, R. J. Dumont, A. Fukuyama, R. Harvey, E. F. Jaeger, K. Indreshkumar, E. Lerche, D. McCune, C. K. Phillips, V. Vdovin, J. Wright, and members of the ITPA-IOS, *Nucl. Fusion* **52**, 023023 (2012); R. Bilato, N. Bertelli, M. Brambilla, R. Dumont, E. F. Jaeger, T. Johnson, E. Lerche, O. Sauter, D. Van Eester, and L. Villard, "Status of the benchmark activity of ICRF full-wave codes

within EUROfusion WPCD and beyond," *AIP Conf. Proc.* **1689**, 060001 (2015).

<sup>5</sup>T. H. Stix, *Waves in Plasmas* (American Institute of Physics, New York, 1992).

<sup>6</sup>D. Smithe, P. Colestock, T. Kammash, and R. Kashuba, *Phys. Rev. Lett.* **60**, 801 (1988).

<sup>7</sup>M. Brambilla and T. Krücken, *Nucl. Fusion* **28**, 1813 (1988).

<sup>8</sup>E. F. Jaeger, L. A. Berry, E. D'Azevedo, D. B. Batchelor, and M. D. Carter, *Phys. Plasmas* **8**, 1573 (2001).

<sup>9</sup>P. T. Bonoli, R. Parker, S. J. Wukitch, Y. Lin, M. Porkolab, J. C. Wright, E. Edlund, T. Graves, L. Lin, J. Liptac, A. Parisot, A. E. Schmidt, V. Tang, W. Beck, R. Childs, M. Grimes, D. Gwinn, D. Johnson, J. Irby, A. Kanojia, P. Koert, S. Marazita, E. Marmar, D. Terry, R. Vieira, G. Wallace, J. Zaks, S. Bernabei, C. Brunkhorse, R. Ellis, E. Fredd, N. Greenough, J. Hosea, C. C. Kung, G. D. Loesser, J. Rushinski, G. Schilling, C. K. Phillips, J. R. Wilson, R. W. Harvey, C. L. Fiore, R. Granetz, M. Greenwald, A. E. Hubbard, I. H. Hutchinson, B. LaBombard, B. Lipschultz, J. Rice, J. A. Snipes, J. Terry, S. M. Wolfe, and Alcator C-Mod Team, *Fusion Sci. Technol.* **51**, 401 (2007).

<sup>10</sup>M. Ono, *Phys. Plasmas* **2**, 4075 (1995).

<sup>11</sup>B. D. Fried and S. D. Conte, *The Plasma Dispersion Relation* (Academic Press, New York, 1961).

<sup>12</sup>D. N. Smithe, *Plasma Phys. Control. Fusion* **31**, 1105 (1989).

<sup>13</sup>J. Hosea, R. E. Bell, B. P. LeBlanc, C. K. Phillips, G. Taylor, E. Valeo, J. R. Wilson, E. F. Jaeger, P. M. Ryan, J. Wilgen, H. Yuh, F. Levinton, S. Sabbagh, K. Tritz, J. Parker, P. T. Bonoli, R. Harvey, and NSTX Team, *Phys. Plasmas* **15**, 056104 (2008).

<sup>14</sup>J. M. Park, private communication.

<sup>15</sup>R. J. Dumont, C. K. Phillips, and D. N. Smith, *Phys. Plasmas* **12**, 042508 (2005).

<sup>16</sup>E. F. Jaeger, L. A. Berry, S. D. Ahern, R. F. Barrett, D. B. Batchelor, M. D. Carter, E. F. D'Azevedo, R. D. Moore, R. W. Harvey, J. R. Myra, D. A. D'Ippolito, R. J. Dumont, C. K. Phillips, H. Okuda, D. N. Smithe, P. T. Bonoli, J. C. Wright, and M. Choi, *Phys. Plasmas* **13**, 056101 (2006); E. F. Jaeger, R. W. Harvey, L. A. Berry, J. R. Myra, R. J. Dumont, C. K. Phillips, D. N. Smithe, R. F. Barrett, D. B. Batchelor, P. T. Bonoli, M. D. Carter, E. F. D'Azevedo, D. A. D'Ippolito, R. D. Moore, and J. C. Wright, *Nucl. Fusion* **46**, S397 (2006).

<sup>17</sup>R. W. Harvey and M. G. McCoy, in *Proceedings of the IAEA Technical Committee Meeting on Simulation and Modeling of Thermonuclear Plasmas, Montreal, Canada* (1992), USDOC NTIS Document No. DE93002962.